Chemical Engineering Journal 448 (2022) 137590

Contents lists available at ScienceDirect

Chemical Engineering Journal

journal homepage: www.elsevier.com/locate/cej

Thermochemical energy applications of green transition metal doped MIL–100(Fe)

Tahmid Hasan Rupam [a,b], Timothy Steenhaut [c], Mujib L. Palash [d], Yaroslav Filinchuk [c], Sophie Hermans [c,*], Bidyut Baran Saha [b,e,*]

[a] International Institute for Carbon-Neutral Energy Research, Kyushu University, 744 Motooka, Nishi-ku, Fukuoka 819-0395, Japan
[b] Green Asia Education Center, Kyushu University, Kasuga-koen 6-1, Kasuga-shi, Fukuoka 816-8580, Japan
[c] Institute of Condensed Matter and Nanosciences (IMCN), UCLouvain, Place Louis Pasteur 1/L4.01.03, 1348 Louvain-la-Neuve, Belgium
[d] Department of Electrical and Electronic Engineering, University of Dhaka, Dhaka 1000, Bangladesh
[e] Mechanical Engineering Department, Kyushu University, 744 Motooka, Nishi-ku, Fukuoka 819-0395, Japan

ARTICLE INFO

Keywords:
Adsorption
Energy storage and conversion
MOFs, surface energy
Transition metals

ABSTRACT

Recently metal organic frameworks (MOFs), already known as adsorbent materials, have gained increasing research interest in thermal energy storage and conversion. MOF-water working pairs have been envisaged to provide the next revolutionary advancement in the existing sorption-based thermal energy storage and conversion systems. Herein, a promising MOF for high water sorption, MIL–100(Fe), and its transition metal-doped (Ni^{2+} and Co^{2+}) derivatives are produced following a green synthesis procedure. The synthesized materials were tested in water sorption measurements using a thermogravimetric technique. The experimentally obtained adsorption data were correlated with the Sun-Chakraborty adsorption isotherm model. As an example of thermal energy conversion, an adsorption chiller is considered, and hence cooling cycles were drawn using the sorption data. The cooling cycles revealed that the nickel-doped MIL–100(Fe) demonstrates the highest value of the specific cooling effect (450.79 kJ kg^{-1}) among the studied MOFs. Inverse gas chromatography technique was employed to investigate the surface free energy of the parent and doped MIL–100(Fe) MOFs. It was found that nickel-doped MIL–100(Fe) had the highest total surface free energy of 105.41 mJ m^{-2}. Surfaces' Lewis acid-base activities and the work of cohesion and adhesion (towards water molecules) were investigated. The surfaces' properties were correlated with the water adsorption isotherms, which can provide crucial information for developing optimal adsorbents targeting water as the adsorbate for an efficient and effective thermal energy storage and conversion system.

1. Introduction

Nowadays, the global energy demand has dramatically increased with rising concerns over existing fuel reserves and environmental degradation. Thermal energy storage and conversion (TESC) systems have been a prominent research focus worldwide because they can reduce our reliance on fossil fuels while also contributing significantly to the use of renewable and waste heat energy, which can help alleviate CO_2 emissions [1]. Additionally, the abundantly available low-grade thermal energy below 200C occupies approximately 36–54% of the total usable primary energy. Its appropriate utilization can mitigate the inconsistency between a lack of thermal energy supply and rising thermal energy demand [2,3].

Generally, materials used for TESC systems can be categorized into four types: sensible heat materials [4], phase changing materials [5], absorption working pairs [6], and solid sorption pairs [7]. Among the above-mentioned types, the solid sorption technology is facilitated by high energy density and low thermal energy loss during the storage and conversion process [8,9]. The solid sorption working pairs can be classified into two major parts: physisorption caused by Van der Waals interactions and chemisorption dominated by complex chemical reactions. Among these two, physisorption has the benefit of being driven by low-grade thermal energies (typically below 100 °C), such as those found in industrial waste heat or solar thermal collectors, which can be easily collected [10]. However, the major drawback of these systems is their enormous sizes, which arises from the low sorption uptake generally observed in popularly used porous adsorbents such as silica gels,

* Corresponding authors.
E-mail addresses: sophie.hermans@uclouvain.be (S. Hermans), saha.baran.bidyut.213@m.kyushu-u.ac.jp (B.B. Saha).

https://doi.org/10.1016/j.cej.2022.137590
Received 23 April 2022; Received in revised form 13 June 2022; Accepted 14 June 2022
Available online 16 June 2022

Nomenclature

c_P	Specific heat capacity [kJ $kg^{-1}K^{-1}$]
F_c	Carrier gas flow rate [kg s^{-1}]
G	Gibbs free energy [kJ kg^{-1}]
H	Adsorption enthalpy [kJ kg^{-1}]
H	Enthalpy [kJ kg^{-1}]
M	Molar mass [g]
N_A	Avogadro number
j	James-Martin correction factor [–]
n	Heterogeneity parameter [–]
P	Pressure [kPa]
P_D	Deformation polarizability [cm^3g^{-1}]
q	Uptake [kg kg^{-1}]
R	Universal gas constant [kJ $kg^{-1}K^{-1}$]
T	Temperature [K]
t	Time [s]
t_0	Dead time [s]
t_R	Retention time [s]
v_n	Retention volume [cm^3g^{-1}]
W	Work of adhesion/cohesion [mJ m^{-2}]

Greek symbols

α	Pre-exponential constant [–]
α_a	Atomic polarizability [–]
α_e	Electronic polarizability [–]
Δ	Difference [–]
γ	Surface energy [mJ m^{-2}]
η	Refractive index [–]
ρ	Molar density [g cm^{-3}]

Superscripts

0	Free state
CH_2	Methylene group
$C_{n+1}H_{2n+4}$	Alkane molecule
D	Dispersive
SP	Specific

Subscripts

ads	Adsorption
adh	Adhesion
coh	Cohesion
cond	Condenser
des	Desorption
evap	Evaporator
f	Fluid
g	Gas
L	Mobile phase/probe
M	MOF
S	Stationary phase
s	Saturation
+	Acidic part
–	Basic part
W	Water

Abbreviation

AAS	Atomic absorption spectroscopy
BET	Brunauer, Emmett and Teller
BJH	Barrett-Joyner-Halenda
COP	Coefficient of performance [–]
DP	Diaphragm pump
FID	Flame ionization detector
GWP	Global warming potential
ICP-OES	Inductively coupled plasma-optical emission spectroscopy
MOF	Metal-organic framework
ODP	Ozone depletion potential
PXRD	Powder X-ray diffraction
RP	Rotary pump
RMSD	Root mean squared deviation
SCE	Specific cooling effect [kJ kg^{-1}]
TESC	Thermal energy storage and conversion
TMP	Turbo molecular pump

zeolites, activated carbons, etc. Fortunately, a new class of porous materials, metal–organic frameworks (MOFs, namely 3D porous materials made of metal centers connected by organic linkers) are emerging as adsorbent materials for TESC applications in recent years [11,12], even though their initial applications were focused on other sorption based applications such as gas purification [13], separation and storage [7,14–16], catalysis [17], gas sensing [18,19], water harvesting [20], pollutant removal [21], desalination[22], etc. When compared with traditional porous adsorbents, MOFs provide advantages with high crystallinity, well-defined porous structures, ultra-large surface areas, facile chemical modifications, and so on [23].

Water is an environmentally benign natural refrigerant, which has a high evaporation enthalpy and a high heat of adsorption when adsorbed into MOFs, which makes it a popular choice as a working fluid in MOF-based TESC systems. Additionally, water has no toxicity and flammability. However, MOFs' hydrothermal and cyclic stabilities have been a major limitation in the practical implementation of large-scale MOF-water paired sorption based-TESC systems. After years of research and cumulative contributions of many researchers, some MOFs such as MOF–801, MOF–841(Zr), MIL–53(Cr), CAU–10(Al)–H, MIL–101(Cr), and MIL–100(Fe) have been developed which are hydrothermally stable with moderate to high water uptakes [24]. Nevertheless, water sorption characteristics of these MOFs are yet to reach a satisfactory level to be implemented in practical TESC applications. Therefore there have been extensive studies on deliberate modifications introduced to the MOFs to enhance their water sorption characteristics [25–27]. Among various modification techniques, secondary metal doping into the MOF structure has been found as one of the easiest solutions to reach improved performance [28–30]. Therefore, in this study, we have focused on MIL–100(Fe) and its transition metal-doped derivatives for TESC applications. Apart from the TESC applications, these green MIL-100(Fe) and its derivatives can also find their applications in other open systems such as desalination[31], water harvesting[20], indoor hygrothermal conditioning[32], etc. Interestingly, the iron on which is based MIL–100(Fe) and its derivatives are cheap, abundant, and non-toxic. Studies have further evidenced that the MOF itself presents good water stability, low toxicity, and the main cost of the material up to now is related to the trimesate linker, which price would likely drop with the emergence of large scale applications [33]. Those arguments justify the study of MIL–100(Fe) materials for the above-mentioned indoor applications.

The study begins with synthesizing the MOFs following a green synthesis protocol proposed by Steenhaut et al. [34]. The secondary transition metals, nickel, and cobalt were introduced into the parent structure in a one-pot doping procedure. Necessary material characterizations, including PXRD and thermal stability testing, were performed. N_2 adsorption/desorption experiments were conducted to investigate the porous properties, while AAS and ICP-OES were done to determine the doping concentrations of the transition metal ions in the modified MOFs. Water sorption capacity onto the MOFs was experimentally obtained thermogravimetrically at different temperatures and pressures. The sorption isotherms were correlated with the Sun-Chakraborty

adsorption isotherm model. To determine the thermal energy storage capacity, adsorption enthalpy of water sorption onto the MOFs was investigated. To check the feasibility of thermochemical energy conversion, an adsorption heat pump was selected, and the cooling capacity and the cooling efficiencies were determined. It is expected that the incorporation of a secondary metal dopant into the structure of a MOF could enhance its water sorption properties [35–37]; however, the ultimate goal of this study is to determine the factors which altered due to the dopant metals that resulted in the enhanced characteristics. Adsorption being a surface phenomenon, it is greatly influenced by Gibbs free surface energies of the adsorbents [38]. Hence to investigate the effects of metal dopants onto the surface free energies of parent MIL–100(Fe), the pristine and modified MOFs were characterized using the inverse gas chromatography technique. Gibbs free energies of adsorption, surfaces' Lewis acid-base constants, and the work of adhesion and cohesion were determined for the studied MOFs. In short, this study focused on the following agendas:

- The green transition metal doped MIL-100(Fe) derivatives were characterized for thermal energy conversion (adsorption cooling) and storage applications.
- Gibbs free surface energies of the studied samples were experimentally measured using inverse gas chromatography.
- The surface energy parameters were correlated with the adsorption isotherm data related to the corresponding samples.

2. Materials

In this study, green synthesized parent and transition metal-doped MIL–100(Fe) metal–organic frameworks have been used as adsorbent materials. Nickel and cobalt metals were chosen as the transition metal dopants, and their salts were added in the precursor solution for synthesizing MIL–100(Fe) at 20 mol% doping in the second metal (introduced amount in the synthesis). The samples were then named as parent MIL–100(Fe), MIL–100(Fe, Ni), and MIL–100(Fe, Co). The detailed synthesis procedures can be found in the works of Steenhaut et al. [34].

After successful synthesis, to investigate the structural consistency of the samples, powder X-ray diffraction (PXRD) data were collected using the STOE STADI P Combi diffractometer utilizing CuKα radiation at 40 kV, 40 mA (the data are given in Figure S1, supplementary file). The PXRD analysis confirmed that the incorporation of metal dopants did not alter the structure of the parent MIL–100(Fe) MOF.

Thermal stability tests were performed using a Mettler Toledo TGA/DSC 3 + STARe system. Prior to the experiment, all the samples were subjected to an isotherm at 27 °C for 15 min before being heated to 900 °C under an airflow of 100 ml min^{-1} at a heating rate of 10 °C min^{-1}. The experimental outcomes suggested that all the samples are thermally stable up to approximately 300 °C (Figure S2), which is adequate for heat pump applications [39]. Additionally, it can also be stated that the doping by transition metals had no effect on the thermal stability of the samples.

N_2 adsorption/desorption isotherms onto the synthesized MOFs were experimentally measured at 77 K utilizing a Micromeritics ASAP 2020 device. Before the experiment, the samples were degassed at 200 °C for 10 h. Results showed that the N_2 adsorption isotherms had a sharp increase at very low relative pressures (P/P_0 less than 0.05), which is a characteristic feature of microporous materials (Figure S3). Hence, it can be concluded that the materials are highly microporous, as expected. Employing the BET method, the surface areas of the studied adsorbent materials were obtained from the isotherm data, as well as the pore volumes and pore size distributions according to the BJH method. Atomic absorption spectroscopy (AAS) and inductively coupled plasma-optical emission spectroscopy (ICP-OES) experiments were conducted to investigate the actual concentration of Co and Ni in the doped samples. The detailed experimental descriptions can be found in the supplementary file. BET surface areas, pore volumes, AAS, and ICP-OES data are summarized in Table 1. From Table 1, it can be seen that doping of Co and Ni ions has resulted in increasing the BET surface areas. The pore size distribution profiles (Figure S3) show that all the samples possess two types of micropores, in accordance with the crystal structure of MIL–100 MOFs, and do not show the presence of mesopores that could indicate the presence of defects. The increased surface areas and pore volumes of the bimetallic samples can be explained by the absence of charge balancing anions in the $M^{II}Fe^{III}$-μ_3O (M = Co or Ni) clusters. The absence of such anions results in the potential removal of three solvent molecules for each bimetallic cluster instead of only two for Fe^{III}–μ_3O, leading to higher surface areas. The results of AAS and ICP-OES analyses are consistent and indicate that the amount of doping metal incorporated into the framework is lower than the concentration that was engaged for the syntheses. This can be explained by the higher affinity of the hard Lewis acidic carboxylate linkers for Fe^{3+} than for Co^{2+} and Ni^{2+}, resulting in preferential incorporation of the former. Nevertheless, significant doping was achieved, attaining 11% in the case of Co and 7% in the case of Ni, which should impact the properties of the obtained materials.

3. Thermogravimetric water adsorption isotherms

Water adsorption isotherms onto the untarnished and doped MIL-100(Fe) were experimentally measured using a thermogravimetric method. The experimental facility used for water adsorption measurement was the Rubotherm: MSB-VG-S2 supplied by MicrotracBEL, Japan. The schematic diagram of the experimental unit is shown in Fig. 1. This apparatus is equipped with a magnetic suspension balance to measure the adsorption uptake thermogravimetrically. There are two isothermal oil baths (Julabo) for controlling the temperatures of the adsorption cell and the evaporator unit. Air baths are included in the system to omit any chances of unnecessary condensation inside the pipes. The measurement accuracy of the magnetic suspension unit is in the range of ± 30 μg with an approximate error of ± 0.002%. The oil circulation baths connected in this system have their temperature stabilities in the order of ± 0.01 °C.

For initiating the experiment, around 90 mg of MOF samples were placed in the adsorption cell and treated at 90 °C for 4 h under vacuum conditions to remove any pre-adsorbed water vapor. A diaphragm pump (DP), a rotary pump (RP), and a turbo molecular pump (TMP) have been employed to achieve the necessary vacuum conditions. After degassing, the dry mass of the samples was noted, and this mass was used for all the computations. After that, Helium gas is passed into the adsorption cell to make the buoyancy corrections. Once the pretreatment, dry mass recording, and buoyancy corrections have been done, the adsorption cell and the evaporator unit are brought to their respective specified temperatures using the oil baths. Once thermal equilibrium is achieved, the adsorption cell and the refrigerant cell are connected by opening the

Table 1
BET surface areas, pore volumes, AAS, and ICP-OES data [34].

Sample name	BET surface area [m^2g^{-1}]	Pore volume [cm^3g^{-1}]	AAS [mol %, Co or Ni]	ICP-OES [mol %, Co or Ni]
MIL–100(Fe)	2048	0.9290	[–]	[–]
MIL–100(Fe, Co)	2256	1.0671	11.4	11.0
MIL–100(Fe, Ni)	2274	1.0369	7.0	7.5

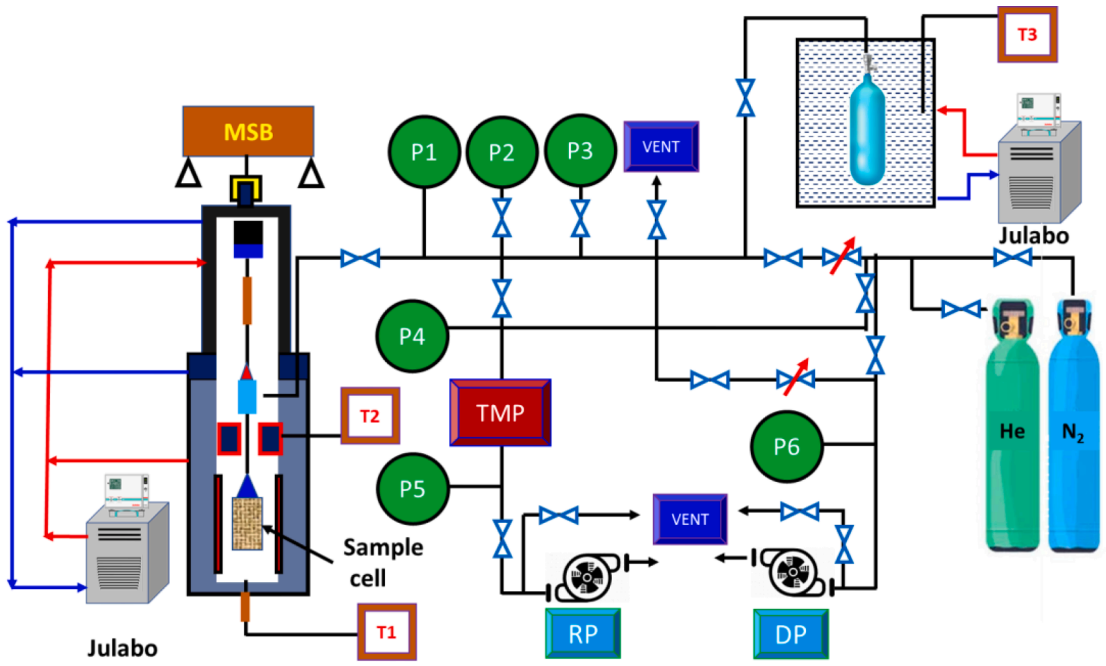

MSB: Magnetic Suspension Balance; RP: Rotary Pump; DP: Diaphragm Pump; TMP: Turbo Molecular Pump; T_i: Temperature sensors, P_i: Pressure sensors

Fig. 1. Schematic diagram of the adsorption measuring unit (Rubotherm: MSB-VG-S2).

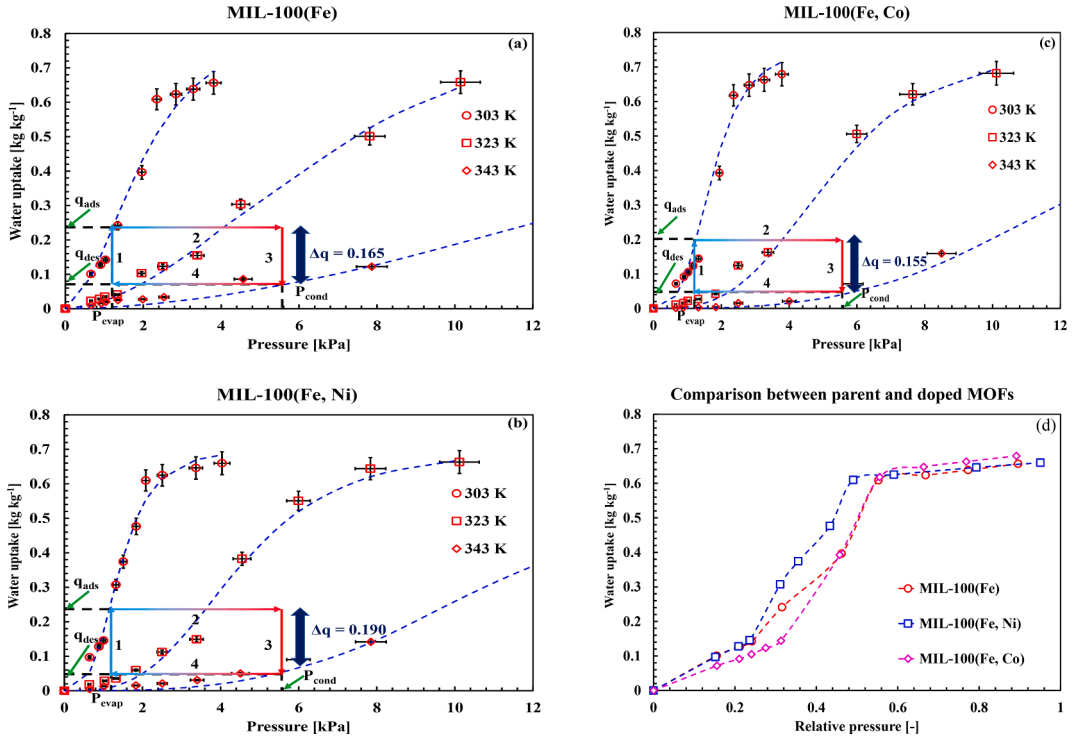

Fig. 2. Water adsorption isotherm data (markers represent the experimental data) correlated with the Sun-Chakraborty adsorption isotherm model (dashed lines) for (a) MIL–100(Fe), (b) MIL–100(Fe, Ni), and (c) MIL–100(Fe, Co) (with an error bar of ± 5%). (d) Comparison of water sorption isotherms onto pristine and modified MIL–100(Fe) MOFs (plotted with respect to relative pressure).

valve to initiate adsorption. The water adsorption data onto the MOFs were measured at three different temperatures 303 K, 323 K, and 343 K, at variable evaporator pressures.

The water adsorption isotherms onto the pristine MIL–100(Fe) and the Co and Ni-doped MIL–100(Fe) were thermogravimetrically obtained at different temperatures with varying evaporator pressures, and the isotherm data are correlated with the Sun-Chakraborty adsorption isotherm model [40] which is given in Eq. (1).

$$q = q^0 \frac{\left\{\alpha \exp\left(\left[n\left(h^0 - h_{fg}\right)\right]/RT\right)\right\}\left(P/P_s\right)^n}{1 + \left\{\alpha \exp\left(\left[n\left(h^0 - h_{fg}\right)\right]/RT\right) - 1\right\}\left(P/P_s\right)^n} \quad (1)$$

Here, q and q^0 are the instantaneous and equilibrium uptakes, whereas h^0 is the zero-uptake adsorption enthalpy. α and n are non-dimensional fitting constants defined as the pre-exponential coefficient and heterogeneity parameter, respectively. The experimental uptake data fitted with the Sun-Chakraborty adsorption isotherm model is depicted in Fig. 2 (a-c). The fitting parameters of the isotherm model are furnished in Table 2. The RMSD error percentage (less than 5%) suggests that the Sun-Chakraborty model correlates with the experimental data reasonably well. Fig. 2 (d) shows the comparison between the water sorption isotherms onto the parent and modified MIL–100(Fe) MOFs.

Fig. 2 (d) shows the effect of metal doping on the green synthesized MIL–100(Fe). Though the equilibrium uptakes are almost similar for the parent and doped samples, in the case of Ni doping, the water adsorption isotherm has shifted in the low-pressure region in the relative humidity range between 0.2 and 0.5. Whereas for Co doping, the isotherm experienced a right shift towards the high-pressure region. The shifting of adsorption isotherm is a crucial parameter in system performance. Usually, a shift in the lower pressure region corresponds to better cooling output as lower evaporative pressures can be reached. On the other hand, a right shift in the pressure scale can provide the advantage of reducing the minimum required regeneration temperature, which enhances the system's efficiency. The water sorption uptake in the green synthesized MIL-100(Fe), and its derivatives are slightly lower than that of the other traditional MIL-100(Fe)'s reported elsewhere[20,41]. The MIL-100(Fe)'s reported by Jeremias et. al.[41], and Maher et. al.[20], had F^- and Cl^- as charge balancing anions, whereas the green synthesized MIL-100(Fe) had OH^-. According to Chen et al., [42] This difference in charge balancing anion can have a significant impact on the water sorption when the relative pressure is less than 1. In their study, they showed that although the saturation uptake (at relative pressure 1) the F^-, Cl^-, and OH^- whichever charge balancing anion is used, the uptake remains the same ar this does not alter the structure of the MOF. However, in the case of OH^- anion, the water uptake at a lower pressure than the saturation pressure can be lower due to the weaker water-structure interactions.

Along with the water adsorption uptake, sorption kinetics were also measured and are provided in the supplementary section (Figure S4). As expected, the adsorption equilibrium time for the studied samples is almost the same. However, a closer look reveals that the water sorption onto the Ni doped sample is slightly faster than the parent one, whereas the kinetics of the Co doped sample is somewhat slower. The difference in kinetics is negligibly small and will not have a major impact on the system performance.

Table 2
Fitting parameters of Sun-Chakraborty adsorption isotherm model.

Fitting parameters	MIL–100(Fe)	MIL–100(Fe, Co)	MIL–100(Fe, Ni)
q^0 [kg kg^{-1}]	0.72	0.73	0.69
h^0 [kJ kg^{-1}]	3295.41	2671.73	2805.95
α [-]	0.02	0.90	0.40
n [-]	0.82	1.45	1.52
RMSD [%]	2.8	3.1	2.3

For a better understanding of the effect of transition metal doping, P-T-q diagrams are drawn into the water adsorption isotherms at different temperatures, as depicted in Fig. 2 (a), (b), and (c). While constructing the P-T-q diagrams, the adsorption and desorption temperatures were considered as 303 K and 343 K, respectively. The evaporative pressure was chosen as 1.2 kPa (Corresponding to a 283 K cooling temperature), whereas the condenser pressure was selected as 5.6 kPa (308 K). The P-T-q cycle has four steps: adsorption, preheating, desorption, and pre-cooling, denoted as 1, 2, 3, and 4, respectively. Similar to other adsorption-based energy conversion systems, the system performance of the adsorption heat pump is directly proportional to the net adsorbate (water) uptake. The net uptake, Δq is defined as the difference between the adsorption uptake and desorption uptake within an operating condition. The net uptakes for MIL–100(Fe), MIL–100(Fe, Ni), and MIL–100 (Fe, Co) are 0.165, 0.190, and 0.155 kg kg^{-1}, respectively.

Another parameter associated with the energetics of an adsorption-based system is the adsorption enthalpy (ΔH_{ads}). The heat produced during the exothermic Van der Waals interaction between the adsorbent and adsorbate molecule is defined as the adsorption enthalpy or isosteric heat of adsorption [43]. For cooling purposes, a lower value of adsorption enthalpy is desired because this adsorption enthalpy denotes the minimum regeneration temperature. A lower value of isosteric heat of adsorption will result in a lower thermal energy requirement for regeneration which will eventually enhance system efficiency. However, for heating applications, a higher isosteric heat of adsorption is desired as the generated heat can be utilized in space heating. Therefore, this study has focused on computing the adsorption enthalpy of the studied pairs as a function of adsorbate loading using Eq. (2).

$$\Delta H_{ads} = h_{fg} - \frac{\left\{\alpha \exp\left(\left[n\left(h^0 - h_{fg}\right)\right]/RT\right)\right\}\left(1 - q/q^0\right)}{\left\{\alpha \exp\left(\left[n\left(h^0 - h_{fg}\right)\right]/RT\right)\right\}\left(1 - q/q^0\right) + q/q^0}\left(h_{fg} - h^0\right) \quad (2)$$

Fig. 3 illustrates the adsorption enthalpy of the studied pairs as a function of water uptake at 303 K. From Fig. 3, it is evident that the isosteric heat of adsorption is a decreasing function of increasing water loading. This is because adsorbates first adsorb in the high energy sites and then gradually move into the adsorption sites having lower energy. A sorption site with high energy usually corresponds to the strongest van der Waals interactions; hence a higher adsorption enthalpy has resulted. The adsorption enthalpy of the parent MIL–100(Fe) is significantly higher than that of the doped MOFs. As the adsorption enthalpy changes with the increase of adsorbate uptake, it can be concluded that the surface of MOFs is energetically heterogeneous. However, the rate of decrement for the parent and doped MOFs are not the same. The

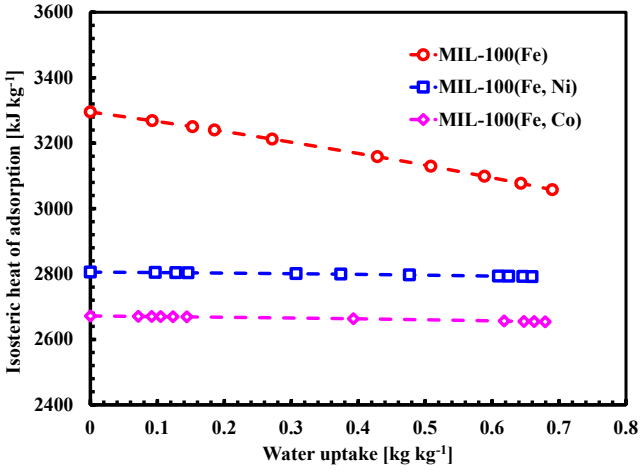

Fig. 3. Isosteric heat of adsorption as a function of water loading at 303 K.

transition metal dopants have caused the adsorption enthalpy to decrease as well as stabilizing the rate of decrement. Therefore, it can be stated that the incorporation of metal dopants has made the MOFs energetically more homogeneous.

Utilizing the adsorption enthalpy and net adsorbate uptake at a fixed operating condition, the energy density of the studied MOFs can be obtained by the following relation:

Energy density $= \Delta H_{ads} *$ Net uptake (Δq).

Using the above formula, the energy density for MIL–100(Fe), MIL–100(Fe, Co), and MIL–100(Fe, Ni) are 528.0 kJ kg^{-1}, 414.63 kJ kg^{-1}, and 532.0 kJ kg^{-1}, respectively. While computing the energy densities, the average values of the adsorption enthalpy were considered.

4. Performance indicators

To investigate the enhancement in system performance induced by deliberate metal doping, it is necessary to analyze the system performance indicators. In the case of adsorption heat pumps, the specific cooling effects and the coefficient of performance are two of the most important system performance indicators to consider in which the first one accounts for the cooling capacity while the latter deals with how efficiently the system can provide the cooling.

Equations (3) [9] and (4) [36] can be utilized for computing the specific cooling effect and coefficient of performance for the parent and doped MIL–100(Fe) MOFs. In Eq. (4), a correction factor of 0.80 has been included to mimic the heat energy losses (20% losses) in the heat exchangers.

$$SCE = (q_{ads} - q_{des})h_{fg}(T_{evap}) + \int_{cond}^{evap} dh_f \tag{3}$$

$$COP = \left\{ \frac{h_{fg}(T,P)}{\Delta H_{ads} + \left\{ c_{p,MOF}/\Delta q (T_{des} - T_{ads}) \right\} + \left[q^0/\Delta q \left\{ c_{p,water}(T_{des} - T_{ads}) \right\} \right]} \right\} \times 0.80 \tag{4}$$

The maximum cooling effect per cycle in adsorption chillers can be assumed to be equal to the refrigerant's latent heat of evaporation, while the minimum heat energy required to drive the system can be approximated as the sum of the adsorption enthalpy and the specific heat capacities of the adsorbent and adsorbate materials. However, in this study, the net sorption uptake is greater than 0.15 kg kg^{-1}; thus, the effects of specific heat capacities will be minimal. Therefore, for simplicity, the heat losses due to the specific heat capacities of MOFs and water were neglected, and the simplified equation for obtaining the COP value takes the following form:

$$COP = \left(\frac{h_{fg}(T,P)}{\Delta H_{ads}(q)} \right) \times 0.80 \tag{5}$$

Eqs. (3) and (5) were used to calculate the specific cooling effect (SCE) and coefficient of performance (COP). Fig. 4 shows the specific cooling effect values of the pristine and modified MIL–100(Fe) MOFs. The parent MIL–100(Fe) has an SCE value of 391.47 kJ kg^{-1}, whereas the Ni-doped sample shows a 15% increment with an SCE value of 450.79 kJ kg^{-1}. However, in the case of Co-doped MIL–100(Fe), there is a 6% reduction in SCE value (367.75 kJ kg^{-1}). The variation of SCE values has resulted from the different values of net uptake for the parent and doped MOFs, Δq obtained from the P-T-q diagrams. The cooling efficiencies were also checked for the studied pairs. The MIL–100(Fe), MIL–100(Fe, Co), and MIL–100(Fe, Ni) showed an average cooling COP of 0.64, 0.75, and 0.76, respectively. The COP values of the studied MOFs are comparable to the popular MOFs studied for adsorption chiller, such as cooling COPs for aluminum fumarate and its transition metal doped derivatives are approximately 0.61 [36], and for MOF-801 and its transition metal doped derivatives, the cooling COPs are approximately 0.63 [44]. The COPs for aluminum fumarate, MOF-801, and their respective derivatives are factored with 0.80 assuming a 20% heat loss in the heat exchangers. The lower COP of the parent MIL–100(Fe) has resulted from the high adsorption enthalpy of the associated pair. For investigating the performance indicators, a working condition of $T_{ads} = 303$ K, $T_{des} = 343$ K, $P_{evap} = 1.2$ kPa, and $P_{cond} = 5.6$ kPa was considered.

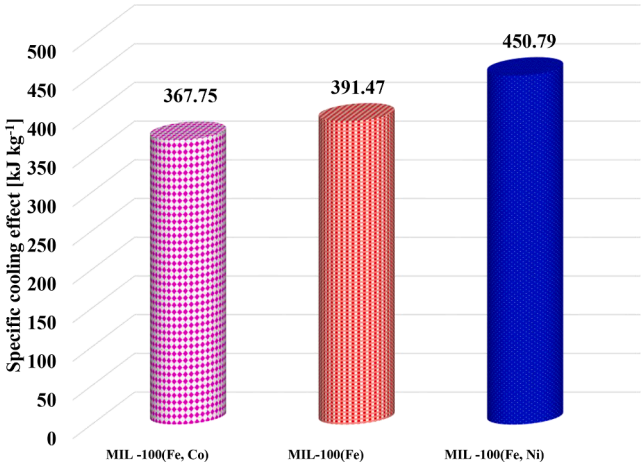

Fig. 4. Comparison of specific cooling effects among the parent and doped MIL–100(Fe) MOFs.

5. Surface chemistry

Transition metal doping has resulted in a favorable outcome in terms of system performance indicators (COP and SCE). Therefore, from an engineering point of view, this work is already a successful one. However, from a scientific viewpoint, there are still some questions, such as why the water adsorption isotherms on the doped samples are altered and the effects of the dopant metals on the adsorption phenomena. In the quest for answers to these questions, the studied MOFs were characterized using inverse gas chromatography to investigate their surface chemical properties.

Inverse gas chromatography experiments were performed using an iGC-SEA (Surface Energy Analyzer) unit supplied by Surface Measurement Systems, UK. The experimental unit is equipped with a flame ionization detector (FID) to detect organic molecules. There are twelve reservoirs where polar and nonpolar probes are kept. Before the experiment, the samples were pre-treated at 120 °C for 24 h under vacuum to remove any moisture contained within their structures. After that, the dry masses of the studied adsorbents were recorded. About 5 mg of each sample (dry) was kept inside a sterilized glass column having an inner diameter of 3 mm and a length of 30 cm. The columns were prepared under mechanical vibration, and the samples were fixed inside the columns with glass wool at both ends of the samples. To remove any physisorbed moisture onto the samples, the columns were then heated at 120 °C for two hours with a carrier gas (helium in this case) flow at 30

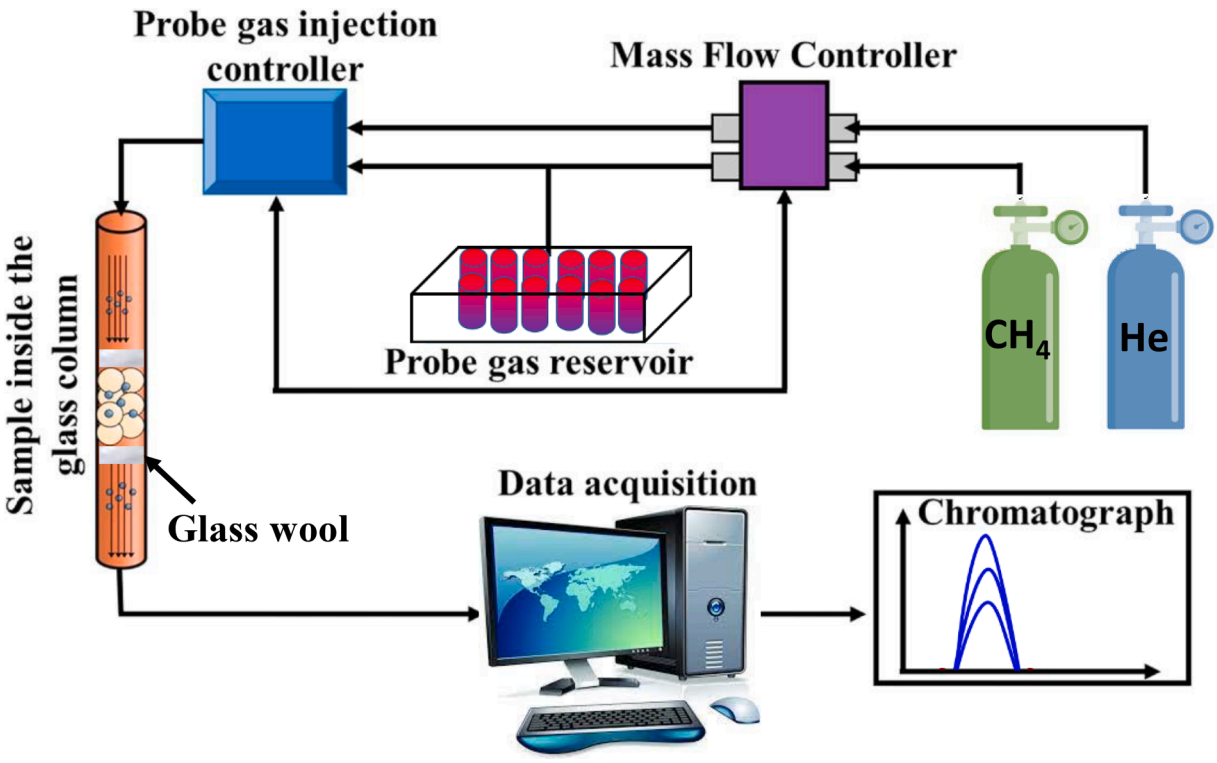

Fig. 5. Schematic diagram of the iGC-SEA experimental unit.

ml/min.

Measurements were carried out at 120 °C with a carrier gas flow rate of 20 ml/min. In this study, four nonpolar probes (hexane, heptane, octane, and nonane) and four polar probes (ethyl acetate, acetone, acetonitrile, and dichloromethane) were used to investigate the surface properties. The properties of the probe molecules are provided in Table S1 in the supplementary section. The probe gasses were transported to the stationary samples by helium (carrier gas), where the probes got adsorbed onto the surface of the adsorbents (MOFs). Later, these adsorbed molecules were eluded from the surface using the same carrier gas and detected through the FID. The schematic diagram of the experimental facility is given in Fig. 5.

The chromatograph recorded in the iGC-SEA contains the information on the retention time (t_r), which is defined as the time required for generating the chromatographic peak after elution. However, this retention time also includes the noninteracting dead time (t_0) taken by the probe molecules to travel from one end of the column to the other. Therefore, the actual interaction or the retention time can be found as $t_r - t_0$. Utilizing this time interval, the retention volume (v_n) of the probe gases can be obtained from Eq. (6).

$$v_n = jF_c(t_r - t_0) \tag{6}$$

Here F_c is the carrier gas flow rate, and j is the James-Martin correction factor compensating for the variations in v_n caused by the pressure drops inside the column and the packing density of the adsorbent material. At equilibrium, the changes in molar Gibbs free energy (ΔG^0) of adsorption and desorption are equal, and hence it can be written as:

$$\Delta G^0_{ads} = \Delta G^0_{des} = RT\ln v_n + C \tag{7}$$

where R is the molar gas constant (8.314 J $mol^{-1}K^{-1}$), and T is the absolute temperature. C is an arbitrary constant designated for the differences in the reference states. The molar Gibbs free energy of adsorption or the surface energy consists of two components: dispersive and specific surface energies. The dispersive surface energy is caused by the nonpolar interactions based on London forces, whereas the specific part is composed of the polar interactions. The changes in Gibbs free energy of adsorption can be written as [45]:

$$\Delta G^0_{ads} = \Delta G^D_{ads} + \Delta G^{SP}_{ads} \tag{8}$$

On the other hand, the change in Gibbs free energy is related to the number of carbon atoms present on the alkane molecules, which can be mathematically expressed as[46]:

$$-\Delta G^0_{ads} = N_A \times A_{cross} \times W_A \tag{9}$$

Here, N_A is the Avogadro's number, A_{cross} is the cross-sectional area of the probes, and WA stands for the work of adhesion of the adsorbent's surface towards the alkane molecules. The work of adhesion has an explicit relation with the dispersive surface energies of the interacting surfaces. According to Fowkes, the work of adhesion as a function of dispersive surface energies of the respective interacting surfaces can be obtained by:

$$W_A = 2\sqrt{\gamma^D_S \times \gamma^D_L} \tag{10}$$

Here γ^D_S and γ^D_L are the dispersive surface energies of the stationary phase (solid porous adsorbent) and the mobile phase (probe molecules). Combining Eqs. (7), (9), and (10) the experimentally measured retention volume can be expressed as a function of surface energy components via the following equation:

$$RT\ln v_n = 2N_A \times A_{cross} \times \sqrt{\gamma^D_S \gamma^D_L} + C \tag{11}$$

In the Dorris-Gray method, the free energy of alkane probes varies linearly with the carbon number in the alkane molecule, and the slope of the linear line determines the free energy component of a single methylene group [47].

According to the Dorris-Gray method, the dispersive surface energy of the stationary phase (MOFs) can be obtained from the following equation:

$$\gamma_S^D = \frac{1}{4\gamma_{CH_2}^D}\left(\frac{-\Delta G_{CH_2}^0}{N_A A_{cross\_CH_2}}\right) \quad (12)$$

However, the Dorris-Gray method is incompatible with determining specific surface energy components; for this purpose polarization method is invoked [48]. The microscopic polarizability (α) of a molecule has two major components: electronic (α_e) and atomic polarizability (α_a). The atomic polarizability is negligibly small; hence it would be $\alpha \cong \alpha_e$ that can be considered.

The molar deformation polarization can be correlated with the free energy of adsorption using the following mathematical expression:

$$RT\ln v_n + C_1 = C_2 P_{DL} P_{DS} + \left(-\Delta G^{SP}\right) \quad (13)$$

Here, C_1 and C_2 are two constants relating to the reference states andP_{DL},P_{DS} are defined as the molar deformation polarization of the mobile and stationary phase, respectively. In the cases of nonpolar alkane probes, the specific interaction energy ΔG^{SP} can be neglected, and then Eq. (16) reduces to the following form:

$$RT\ln v_n + C_1 = C_2 P_{DL} P_{DS} \quad (14)$$

$RT\ln v_n$ varies linearly with changing P_{DL}, and the slope of the straight line is $C_2 P_{DS}$ which is proportional to the straight line obtained from the Dorris-Gray method. Polar probes have both dispersive and specific interactions. Therefore, the Gibbs free energy resulting from the specific interactions can be obtained from the vertical distances between the $RT\ln v_n$ points and the straight line resulting from the dispersive interactions. The plots of $RT\ln V_n$ versus the molar deformation polarization are given in Figure S5. in the supplementary section.

5.1. Surface energy

Gibbs free energies of the nonpolar probes were determined using the Dorris-Gray method, whereas, for polar probes, the polarization method was utilized. For both cases, surface coverage of 0.01 was chosen. In the polarization method, for obtaining the specific surface energy part, the Della Volpe scale [49] was employed where two polar probes, ethyl acetate (γ_L^-=475.67 mJ m^{-2} andγ_L^+ = 0 mJ m^{-2}) and dichloromethane (γ_L^-=0 mJ m^{-2} andγ_L^+ = 124.58 mJ m^{-2}) were used [50]. The alkane lines along with the Gibbs free energies of the polar probes can be found in the supplementary section (Figure S4 (a-c)). The dispersive and specific surface energies of the parent and doped MIL–100(Fe) are illustrated in Fig. 6.

It is evident from Fig. 6. that the transition metal doping has altered the nature of the surface of MIL–100(Fe) MOF. In the case of Co doping, the specific surface energy almost had no change, whereas the dispersive surface energy experienced a significant reduction. This decrement in the dispersive surface energy, as well as the total surface energy (73.08 mJ m^{-2}), might be responsible for lower water uptake in MIL–100(Fe, Co) sample in the pressure regions 0.01 to 0.4 RH (see Fig. 2 (d)). On the other hand, Ni doping has increased the specific surface energy around two folds while keeping the dispersive surface energy almost unchanged. As a result, the total surface energy in the Ni-doped MIL–100 (Fe) MOF is the highest among the studied samples (105.41 mJ m^{-2}), and consequently, this sample exhibits the highest water sorption uptake in the working pressure region. Therefore, it can be concluded that the total surface energy (combining the dispersive and specific surface energies) has a direct relationship with the water uptake in the working region.

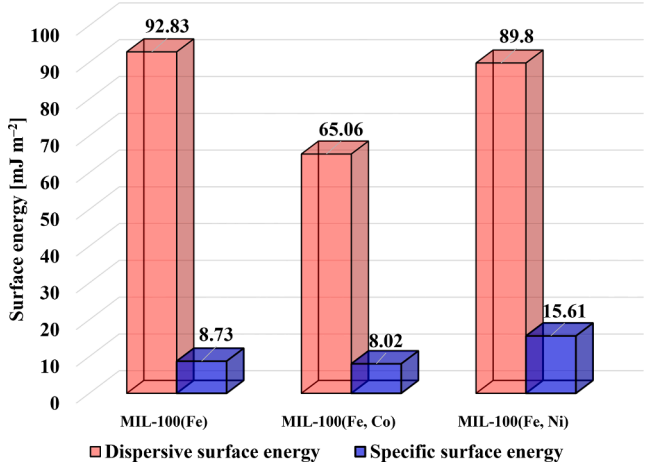

Fig. 6. Comparison of dispersive and specific surface energies among parent and transition metal-doped MIL–100(Fe) MOFs.

5.2. Surface Lewis acidity/basicity

Once the specific surface energy is determined, the surface's Lewis acid-base activities can be obtained using Gutmann's approach via Eq. (18).

$$-\frac{\Delta G^{SP}}{AN^*} = \left(\frac{DN}{AN^*}\right)K_a + K_b \quad (18)$$

Here, DN and AN* are the donor and corrected acceptor numbers of the polar probes. The exact values of DN and AN* are furnished in Table S1. The slope and y-axis intercept from their respective plots of ΔG^{SP} as a function of DN/AN* presented in Fig. 7 can be used to derive the Lewis acid and base constants of the examined MOFs. Table 3 lists the Lewis acid and base constants of the various MOFs. From Table 3, it can be concluded that all of the MOFs studied in this study have a surface that responds like a Lewis base since the K_a/K_b ratio is less than 1. The prevailing base constant indicates that the adsorbent's surface will first interact mostly with the H^+ component of water.

5.3. Work of cohesion and work of adhesion

The affinity of any MOF to capture water molecules is indicated by its work of adhesion with water, whereas the work of cohesion indicates the compressibility of the adsorbent material, which is required for a compact system. The total work of cohesion or adhesion comprises two components, according to the Fowkes equation: dispersive component γ_D (resulting from Lifshitz-van der Waals interactions) and specific component γ_{SP} (resulting from acid-base interactions) [51,52]. As a result, the total work of adhesion and/or cohesion can be expressed as:

$$W_{adh/coh} = \gamma_D + \gamma_{SP} \quad (19)$$

Neglecting the irreversible interactions, the work of adhesion and

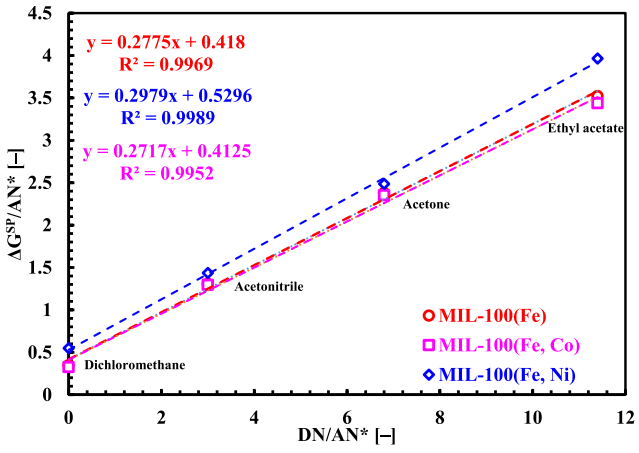

Fig. 7. Determination of Lewis acid-base constants for the parent and modified MIL–100(Fe) MOFs via the Gutmann approach.

Table 3
Lewis acid-base constants for the studied MOFs.

Sample	Lewis acid constant, K_a [–]	Lewis base constant, K_b [–]	K_a/K_b [–]
MIL–100(Fe)	0.2775	0.4180	0.6639
MIL–100(Fe, Co)	0.2717	0.4125	0.6587
MIL–100(Fe, Ni)	0.2979	0.5296	0.5625

Table 4
Surface energy components and work of adhesion and cohesion.

Sample	Dispersive surface energy [mJ m^{-2}]	Specific surface energy [mJ m^{-2}]		Work of adhesion [mJ m^{-2}]		Work of cohesion [mJ m^{-2}]	
	γ_D	γ_+	γ_-	$\gamma_{D,adh}$	$\gamma_{SP,adh}$	$\gamma_{D,coh}$	$\gamma_{SP,coh}$
MIL–100(Fe)	92.83	6.50	2.93	89.97	43.05	185.65	17.47
MIL–100(Fe, Co)	65.06	6.19	2.60	75.32	41.40	130.13	16.04
MIL–100(Fe, Ni)	89.80	8.24	7.39	88.49	56.45	179.61	31.22

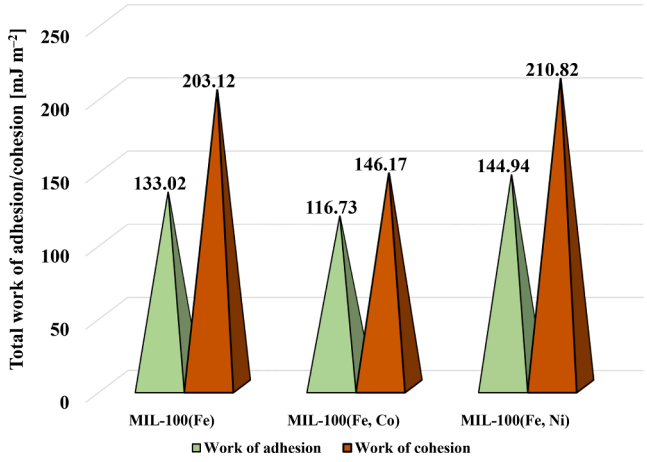

Fig. 8. Total work of adhesion (towards water) and cohesion for the parent and modified MIL–100(Fe) MOFs.

cohesion can be obtained by the geometric means of the surface energies of the interacting materials. Therefore, the total work of adhesion and cohesion of the studied materials can be computed using the following equations:

$$W_{adh} = 2\left[\gamma_D^M \gamma_D^W + \sqrt{\gamma_+^M \gamma_-^W} + \sqrt{\gamma_-^M \gamma_+^W}\right] \quad (20)$$

$$W_{coh} = 2\left[\gamma_D^M + \sqrt{\gamma_+^M \gamma_-^M} + \sqrt{\gamma_-^M \gamma_+^M}\right] \quad (21)$$

Here, according to Good and Oss's suggestion, the specific component γ_{SP} has been replaced with an acid and base parameter γ_+ and γ_-, respectively [53]. The 'M' and 'W' superscripts indicate that the components are associated with the MOF or water, respectively.

The individual surface energy components are tabulated in Table 4. The total work of adhesion and cohesion of the studied samples for a surface coverage of 0.01 are depicted in Fig. 8.

It is evident from Table 4 and Fig. 8 that Co^{2+} doping has caused the work of adhesion and cohesion in the modified MOF to decrease, whereas, in the case of Ni^{2+} a slight increase is observed. A closer inspection of Table 4 suggests that the incorporation of Ni^{2+} and Co^{2+} in the structure of pristine MIL–100(Fe) has reduced the dispersive work of adhesion (towards water), which is reflected by the decrement of adsorption enthalpy shown in Fig. 3. The lower dispersive work of adhesion has resulted in weaker exothermic Van der Waals interactions, which caused the adsorption enthalpy to decrease. On the other hand, the increase in the specific component of the work of adhesion in the case of Ni^{2+} doped MIL–100(Fe) might have caused a higher amount of water molecules to get adsorbed in the pores; which in turn provided the additional nucleon sites for the water cluster formation in the steeper uptake region (Fig. 2(d)). Additionally, the Ni^{2+} incorporated MOF had a higher work of cohesion which suggests that this MOF can be utilized more easily in making compressed, consolidated adsorbents that will offer enhanced volumetric water uptake and higher thermal conductivity.

6. Conclusions

In this study, MIL–100(Fe) and transition metal doped MIL–100(Fe, Ni) and MIL–100(Fe, Co) metal–organic frameworks were successfully synthesized following a green synthesis procedure. The doped samples offered higher BET surface areas of 2256 m^2g^{-1} and 2274 m^2g^{-1} for cobalt and nickel doped MIL–100(Fe) MOFs, respectively, when compared with the parent one (2048 m^2g^{-1}).

The water adsorption isotherms onto the parent and modified MIL–100(Fe) MOFs were experimentally obtained using a thermogravimetric measurement technique at three different temperatures of 30 °C, 50 °C, and 70 °C with varying evaporative pressures. The Sun and Chakraborty model for adsorption isotherms was used to correlate the experimental data with an RMSD error of around ± 3%. P-T-q diagrams were drawn using the adsorption isotherms data to get the net water uptake within an operating condition of T_{ads} = 303 K, T_{des} = 343 K, P_{evap} = 1.2 kPa, and P_{cond} = 5.6 kPa. Under a similar condition, the specific cooling effects were calculated and the values obtained are 391.47 kJ kg^{-1}, 450.79 kJ kg^{-1}, and 367.75 kJ kg^{-1} for the parent, nickel, and cobalt doped MOFs, respectively. The nickel doped MIL–100 (Fe) showed the highest SCE value (450.79 kJ kg^{-1}) because of the highest net uptake it possesses within the considered working pressure range. This SCE value is comparable to the values obtained for other potential MOFs, such as aluminum fumarate (499 kJ kg^{-1})[36] or MOF–801 (373 kJ kg^{-1}) [39], and is significantly higher than the SCE values obtained for traditional adsorbents like silica gels (around 310 kJ kg^{-1}). The energy density for MIL 100(Fe), MIL 100(Fe, Co), and MIL 100(Fe, Ni) are 528.0 kJ kg^{-1}, 414.63 kJ kg^{-1}, and 532.0 kJ kg^{-1}, respectively.

Inverse gas chromatography technique was employed to investigate the surface Gibbs free energies of the pristine and modified MOFs at a specific surface coverage of 0.01. The Co^{2+} doped MIL–100(Fe) has a lower value (73.08 mJ m^{-2}) of total surface energy than the unmodified MIL–100(Fe) (101.56 mJ m^{-2}), whereas Ni^{2+} doping has caused the surface energy of the modified MOF (105.41 mJ m^{-2}) to exceed the parent one. Lewis acid and base constants were investigated using Gutmann's approach for all the studied MOFs. The study revealed that all of the studied MOFs have a surface acting as a Lewis base. Transition metal doping has not significantly altered the acid-base characteristics

in the MOFs. Work of cohesion and work of adhesion towards water was also obtained for the parent and doped MIL–100(Fe) MOFs. Co^{2+} doping has resulted in a decrement of work of adhesion and cohesion; however, in the case of Ni^{2+} doping, an increment in both the work of adhesion and cohesion was observed. This increase in work of adhesion towards water molecules might have caused the nickel-doped sample to have a higher net uptake, which resulted in a higher specific cooling effect. This study includes both experimental and theoretical analyses on how different features of porous materials can affect the systems performance of the thermal energy conversion system. Approaches were made to correlate the experimentally obtained surface energy data with the water adsorption phenomena onto the porous MOFs. The results indicate that an optimum MOF adsorbent can be designed by modifying the organic linker with hydrophilic functional groups, which can enable the sample to have higher work of adhesion toward water. This can be achieved by increasing the surface acidity, which will trigger the enhancement in specific Gibbs free energy. These findings will be crucial for designing optimum porous materials for next generation thermal energy utilization systems.

7. Data availability

The raw/processed data required to reproduce these findings cannot be shared at this time as the data also forms part of an ongoing study.

Declaration of Competing Interest

The authors declare that they have no known competing financial interests or personal relationships that could have appeared to influence the work reported in this paper.

Data availability

Data will be made available on request.

Acknowledgments

A part of this work is financially supported by the Japan Society for the Promotion of Science (JSPS) under project no. 21J12849. We also acknowledge the F.R.S.-FNRS for the FRIA fellowship of TS.

Appendix A. Supplementary data

Supplementary data to this article can be found online at https://doi.org/10.1016/j.cej.2022.137590.

References

[1] H. Zondag, B. Kikkert, S. Smeding, R. de Boer, M. Bakker, Prototype thermochemical heat storage with open reactor system, Appl. Energy. 109 (2013) 360–365, https://doi.org/10.1016/j.apenergy.2013.01.082.
[2] I. Gur, K. Sawyer, R. Prasher, Searching for a better thermal battery, Science 335 (2012) 1454–1455, https://doi.org/10.1126/science.1218761.
[3] C. Forman, I.K. Muritala, R. Pardemann, B. Meyer, Estimating the global waste heat potential, Renew. Sustain. Energy Rev. 57 (2016) 1568–1579, https://doi.org/10.1016/j.rser.2015.12.192.
[4] T. Arunkumar, R. Jayaprakash, A. Ahsan, D. Denkenberger, M.S. Okundamiya, Effect of water and air flow on concentric tubular solar water desalting system, Appl. Energy. 103 (2013) 109–115, https://doi.org/10.1016/j.apenergy.2012.09.014.
[5] H. Maher, K.A. Rocky, R. Bassiouny, B.B. Saha, Synthesis and thermal characterization of paraffin-based nanocomposites for thermal energy storage applications, Therm. Sci. Eng. Prog. 22 (2021), 100797, https://doi.org/10.1016/j.tsep.2020.100797.
[6] Q. Wang, Y. Liu, J. Luo, S. Wang, J. Tang, X. Xu, G. Chen, Theoretical investigations on the cycle performance of a single-pressure diffusion absorption heat transformer with LiBr–H2O-R134a-TEGDME, J. Clean. Prod. 277 (2020), 123303, https://doi.org/10.1016/j.jclepro.2020.123303.
[7] N. Makhanya, B. Oboirien, J. Ren, N. Musyoka, A. Sciacovelli, Recent advances on thermal energy storage using metal-organic frameworks (MOFs), J. Energy Storage. 34 (2021), 102179, https://doi.org/10.1016/j.est.2020.102179.
[8] G. An, Y. Zhang, L. Wang, B. Zhang, An advanced composite sorbent with high thermal stability and superior sorption capacity without hysteresis for a better thermal battery, J. Mater. Chem. A. 8 (2020) 11849–11858, https://doi.org/10.1039/D0TA01320J.
[9] T.H. Rupam, M.A. Islam, A. Pal, B.B. Saha, Adsorption thermodynamics and performance indicators of selective adsorbent/refrigerant pairs, Appl. Therm. Eng. 175 (2020), 115361, https://doi.org/10.1016/j.applthermaleng.2020.115361.
[10] K.A. Rocky, A. Pal, T.H. Rupam, Nasruddin, B.B. Saha, Zeolite-graphene composite adsorbents for next generation adsorption heat pumps, Microporous Mesoporous Mater. 313 (2021) 110839.
[11] T. Qiu, Z. Liang, W. Guo, H. Tabassum, S. Gao, R. Zou, Metal-organic framework-based materials for energy conversion and storage, ACS Energy Lett. 5 (2020) 520–532, https://doi.org/10.1021/acsenergylett.9b02625.
[12] G. An, X. Xia, S. Wu, Z. Liu, L. Wang, S. Li, Metal-organic frameworks for ammonia-based thermal energy storage, Small. 17 (2021) 2102689, https://doi.org/10.1002/smll.202102689.
[13] G. Avci, S. Velioglu, S. Keskin, High-throughput screening of MOF adsorbents and membranes for H2 purification and CO2 capture, ACS Appl. Mater. Interfaces. 10 (2018) 33693–33706, https://doi.org/10.1021/acsami.8b12746.
[14] K. Srinivasu, S.K. Ghosh, Tuning the metal binding energy and hydrogen storage in alkali metal decorated MOF-5 through boron doping: A theoretical investigation, J. Phys. Chem. C. 115 (2011) 16984–16991, https://doi.org/10.1021/jp2035218.
[15] J. Purewal, D. Liu, A. Sudik, M. Veenstra, J. Yang, S. Maurer, U. Müller, D.J. Siegel, Improved hydrogen storage and thermal conductivity in high-density MOF-5 composites, J. Phys. Chem. C. 116 (2012) 20199–20212, https://doi.org/10.1021/jp305524f.
[16] S. Kayal, B. Sun, A. Chakraborty, Study of metal-organic framework MIL-101(Cr) for natural gas (methane) storage and compare with other MOFs (metal-organic frameworks), Energy. 91 (2015) 772–781, https://doi.org/10.1016/j.energy.2015.08.096.
[17] Y.-B. Huang, J. Liang, X.-S. Wang, R. Cao, Multifunctional metal–organic framework catalysts: synergistic catalysis and tandem reactions, Chem. Soc. Rev. 46 (2017) 126–157, https://doi.org/10.1039/C6CS00250A.
[18] X.-F. Wang, X.-Z. Song, K.-M. Sun, L. Cheng, W. Ma, MOFs-derived porous nanomaterials for gas sensing, Polyhedron 152 (2018) 155–163, https://doi.org/10.1016/J.POLY.2018.06.037.
[19] M. Wang, T. Hou, Z. Shen, X. Zhao, H. Ji, MOF-derived Fe2O3: Phase control and effects of phase composition on gas sensing performance, Sensors Actuators B Chem. 292 (2019) 171–179, https://doi.org/10.1016/J.SNB.2019.04.124.
[20] H. Maher, T.H. Rupam, K.A. Rocky, R. Bassiouny, B.B. Saha, Silica gel-MIL 100(Fe) composite adsorbents for ultra-low heat-driven atmospheric water harvester, Energy. 238 (2022), 121741, https://doi.org/10.1016/j.energy.2021.121741.
[21] A. Bathla, S.A. Younis, B. Pal, K.-H. Kim, Recent progress in bimetallic nanostructure impregnated metal-organic framework for photodegradation of organic pollutants, Appl. Mater. Today. 24 (2021), 101105, https://doi.org/10.1016/j.apmt.2021.101105.
[22] M. Kadhom, B. Deng, Metal-organic frameworks (MOFs) in water filtration membranes for desalination and other applications, Appl. Mater. Today. 11 (2018) 219–230, https://doi.org/10.1016/j.apmt.2018.02.008.
[23] M.L. Palash, I. Jahan, T.H. Rupam, S. Harish, B.B. Saha, Novel technique for improving the water adsorption isotherms of metal-organic frameworks for performance enhancement of adsorption driven chillers, Inorganica Chim. Acta. 501 (2020), 119313, https://doi.org/10.1016/j.ica.2019.119313.
[24] M.F. de Lange, K.J.F.M. Verouden, T.J.H. Vlugt, J. Gascon, F. Kapteijn, Adsorption-driven heat pumps: the potential of metal-organic frameworks, Chem. Rev. 115 (2015) 12205–12250, https://doi.org/10.1021/acs.chemrev.5b00059.
[25] A. Karmakar, V. Prabakaran, D. Zhao, K.J. Chua, A review of metal-organic frameworks (MOFs) as energy-efficient desiccants for adsorption driven heat-transformation applications, Appl. Energy. 269 (2020), 115070, https://doi.org/10.1016/j.apenergy.2020.115070.
[26] J. Canivet, A. Fateeva, Y. Guo, B. Coasne, D. Farrusseng, Water adsorption in MOFs: Fundamentals and applications, Chem. Soc. Rev. 43 (2014) 5594–5617, https://doi.org/10.1039/c4cs00078a.
[27] H.J. An, M. Sarker, D.K. Yoo, S.H. Jhung, Water adsorption/desorption over metal-organic frameworks with ammonium group for possible application in adsorption heat transformation, Chem. Eng. J. 373 (2019) 1064–1071, https://doi.org/10.1016/j.cej.2019.05.121.
[28] S. Li, Y. Gao, N. Li, L. Ge, X. Bu, P. Feng, Transition metal-based bimetallic MOFs and MOF-derived catalysts for electrochemical oxygen evolution reaction, Energy Environ. Sci. 14 (2021) 1897–1927, https://doi.org/10.1039/D0EE03697H.
[29] X. Yang, Q. Xu, Bimetallic metal-organic frameworks for gas storage and separation, Cryst. Growth Des. 17 (2017) 1450–1455, https://doi.org/10.1021/acs.cgd.7b00166.
[30] M. Lan, R.-M. Guo, Y. Dou, J. Zhou, A. Zhou, J.-R. Li, Fabrication of porous Pt-doping heterojunctions by using bimetallic MOF template for photocatalytic hydrogen generation, Nano Energy 33 (2017) 238–246, https://doi.org/10.1016/j.nanoen.2017.01.046.
[31] R. AL-Dadah, S. Mahmoud, E. Elsayed, P. Youssef, F. Al-Mousawi, Metal-organic framework materials for adsorption heat pumps, Energy. 190 (2020) 116356.
[32] S. Cui, M. Qin, A. Marandi, V. Steggles, S. Wang, X. Feng, F. Nouar, C. Serre, Metal-organic frameworks as advanced moisture sorbents for energy-efficient high temperature cooling, Sci. Rep. 8 (2018) 15284, https://doi.org/10.1038/s41598-018-33704-4.
[33] G. Chen, X. Leng, J. Luo, L. You, C. Qu, X. Dong, H. Huang, X. Yin, J. Ni, In vitro toxicity study of a porous iron(III) metal-organic framework, Molecules 24 (7) (2019) 1211.

[34] T. Steenhaut, S. Hermans, Y. Filinchuk, Green synthesis of a large series of bimetallic MIL-100(Fe, M) MOFs, New J. Chem. 44 (2020) 3847–3855, https://doi.org/10.1039/d0nj00257g.
[35] A.K. Adhikari, K.-S. Lin, Improving CO2 adsorption capacities and CO2/N2 separation efficiencies of MOF-74(Ni, Co) by doping palladium-containing activated carbon, Chem. Eng. J. 284 (2016) 1348–1360, https://doi.org/10.1016/J.CEJ.2015.09.086.
[36] T.H. Rupam, M.L. Palash, M.A. Islam, B.B. Saha, Transitional metal-doped aluminum fumarates for ultra-low heat driven adsorption cooling systems, Energy. 238 (2022), 122079, https://doi.org/10.1016/j.energy.2021.122079.
[37] H.W.B. Teo, A. Chakraborty, S. Kayal, Post synthetic modification of MIL-101(Cr) for S-shaped isotherms and fast kinetics with water adsorption, Appl. Therm. Eng. 120 (2017) 453–462, https://doi.org/10.1016/J.APPLTHERMALENG.2017.04.018.
[38] T.H. Rupam, M.L. Palash, A. Chakraborty, B.B. Saha, Insights of the adsorbents surface chemical properties effect on water adsorption isotherms, Int. J. Heat Mass Transf. 192 (2022), 122842, https://doi.org/10.1016/j.ijheatmasstransfer.2022.122842.
[39] I. Jahan, T.H. Rupam, M. Palash, K.A. Rocky, B.B. Saha, Energy efficient green synthesized MOF-801 for adsorption cooling applications, J. Mol. Liq. 345 (2022), 117760, https://doi.org/10.1016/j.molliq.2021.117760.
[40] B. Sun, A. Chakraborty, Thermodynamic formalism of water uptakes on solid porous adsorbents for adsorption cooling applications, Appl. Phys. Lett. 104 (20) (2014) 201901.
[41] F. Jeremias, A. Khutia, S.K. Henninger, C. Janiak, MIL-100(Al, Fe) as water adsorbents for heat transformation purposes—a promising application, J. Mater. Chem. 22 (2012) 10148–10151, https://doi.org/10.1039/C2JM15615F.
[42] Y.-R. Chen, K.-H. Liou, D.-Y. Kang, J.-J. Chen, L.-C. Lin, Investigation of the water adsorption properties and structural stability of MIL-100(Fe) with different anions, Langmuir 34 (2018) 4180–4187, https://doi.org/10.1021/acs.langmuir.7b04399.
[43] M.L. Palash, T.H. Rupam, A. Pal, A. Chakraborty, B.B. Saha, R. Wang, Design principles for synthesizing high grade activated carbons for adsorption heat pumps, Chem. Eng. J. Adv. 6 (2021), 100086, https://doi.org/10.1016/j.ceja.2021.100086.
[44] I. Jahan, M.A. Islam, T.H. Rupam, M.L. Palash, K.A. Rocky, B.B. Saha, Enhanced water sorption onto bimetallic MOF-801 for energy conversion applications, Sustain. Mater. Technol. 32 (2022) e00442. https://doi.org/https://doi.org/10.1016/j.susmat.2022.e00442.
[45] H. Balard, E. Brendle, E. Papirer, Determination of the acid-base properties of solid surfaces using inverse gas chromatography: advantages and limitations, acid-base interact, Relev. to Adhes. Sci. Technol. 2 (2000) 299–316.
[46] A. Voelkel, Inverse gas chromatography in the examination of acid-base and some other properties of solid materials, Stud. Surf. Sci. Catal. 99 (1996) 465–477, https://doi.org/10.1016/s0167-2991(06)81031-1.
[47] G.M. Dorris, D.G. Gray, Adsorption of n-alkanes at zero surface coverage on cellulose paper and wood fibers, J. Colloid Interface Sci. 77 (1980) 353–362, https://doi.org/10.1016/0021-9797(80)90304-5.
[48] S. Dong, M. Brendlé, J.B. Donnet, Study of solid surface polarity by inverse gas chromatography at infinite dilution, Chromatographia 28 (1989) 469–472, https://doi.org/10.1007/BF02261062.
[49] C.D. Volpe, S. Siboni, Some reflections on acid-base solid surface free energy theories, J. Colloid Interface Sci. 195 (1997) 121–136, https://doi.org/10.1006/jcis.1997.5124.
[50] M.L. Palash, A. Pal, T.H. Rupam, B.-D. Park, B.B. Saha, Surface energy characterization of different particulate silica gels at infinite dilution, Colloids Surfaces A Physicochem. Eng. Asp. 603 (2020), 125209, https://doi.org/10.1016/j.colsurfa.2020.125209.
[51] P. Mukhopadhyay, H.P. Schreiber, Aspects of acid-base interactions and use of inverse gas chromatography, Colloids Surfaces A Physicochem. Eng. Asp. 100 (1995) 47–71, https://doi.org/10.1016/0927-7757(95)03137-3.
[52] F.M. Fowkes, Calculation of work of adhesion by pair potential suummation, J. Colloid Interface Sci. 28 (1968) 493–505, https://doi.org/10.1016/0021-9797(68)90082-9.
[53] C.J. van Oss, R.J. Good, M.K. Chaudhury, Additive and nonadditive surface tension components and the interpretation of contact angles, Langmuir 4 (1988) 884–891, https://doi.org/10.1021/la00082a018.